Document Version
Final published version

Citation (APA)
Wapperom, M., Taghinejad, S. M., Lyu, X., Farajzadeh, R., & Voskov, D. (2026). A thermodynamically consistent simulation of gas hydrates in porous media using Operator-Based Linearization. *Energy Conversion and Management: X*, *30*, Article 101616. https://doi.org/10.1016/j.ecmx.2026.101616

Energy Conversion and Management: X 30 (2026) 101616

Contents lists available at ScienceDirect

Energy Conversion and Management: X

journal homepage: www.sciencedirect.com/journal/energy-conversion-and-management-x

A thermodynamically consistent simulation of gas hydrates in porous media using Operator-Based Linearization

Michiel Wapperom [a], Sadegh M. Taghinejad [a], Xiaocong Lyu [b], Rouhi Farajzadeh [a,c], Denis Voskov [a,d,*]

[a] Department of Geoscience and Engineering, TU Delft, Delft, Netherlands
[b] China University of Petroleum (Beijing), China
[c] Shell Development Oman LLC, Muscat, Oman
[d] Department of Energy Science & Engineering, Stanford University, CA, USA

ARTICLE INFO

Keywords:
Gas hydrates
Operator-Based Linearization
Thermodynamics
Kinetics
Carbon storage

ABSTRACT

In this work, we present a kinetic simulation model for gas hydrates in porous media using the Operator-Based Linearization (OBL) technique. The OBL approach introduces algebraic operators that represent the physical terms in the mass and energy balance equations. Operators are calculated only in supporting points comprising the discretized parameter space, and operator values and partial derivatives for linear system assembly are readily obtained through (multi-)linear interpolation. Taking advantage of this setup, the implementation of advanced thermodynamic models for hydrate formation and dissociation under kinetic assumptions is simplified. We test the assumptions for thermodynamic modelling by analysing the Gibbs energy surfaces of the fluid and hydrate phases and demonstrate that, in the limit, the thermodynamic equilibrium for both kinetic and equilibrium reaction models is equivalent. We compare the simulation results with the published experimental results for CH_4-hydrates and extend the assessment to a CO_2-hydrate formation experiment in a semi-batch, constant-pressure configuration. The model reproduces the main pressure–temperature transients and hydrate evolution for both CH_4- and CO_2-systems. We demonstrate applicability at core scale for hydrate formation and, at field scale, for gas production from CH_4-hydrates by thermal stimulation and depressurization. The interaction of thermal-compositional phenomena (phase changes, adiabatic expansion, kinetic rates, and reaction enthalpy) gives rise to highly nonlinear physics that an appropriate OBL discretization resolves. Overall, the patterns of hydrate formation and dissociation are highly sensitive to the kinetic-rate inputs; hence, the appropriate choice of the reaction model remains a key consideration from both physical and numerical perspectives.

1. Introduction

Gas hydrates are crystalline solids, composed of hydrogen-bonded water, stabilized by small non-polar guest molecules [1]. The hydrate cages exist in a stable thermodynamic state at sufficient pressure and low-temperature conditions yet above the freezing point of water. Hydrates are a well-known challenge in subsurface engineering, hydrocarbon production, and pipeline transport [2]. With the advent of carbon sequestration in depleted or low-pressure oil and gas fields, the potential for near-wellbore CO_2 (carbon dioxide) hydrate formation has become an operational concern. Injection of dense-phase CO_2 into depleted reservoirs introduces additional hydrate risks. A temperature decrease due to Joule–Thomson cooling and phase transitions during expansion in combination with the availability of water in the reservoir can drive near-wellbore CO_2-hydrate formation, severely impairing injectivity [3,4].

Methane (CH_4) is the most commonly occurring guest molecule in natural hydrate deposits, found typically in continental margin sediments and shallow permafrost [5]. Estimates of gas in place in the form of hydrates range over a few orders of magnitude, but even in the most modest estimates they represent a substantial portion of mobile carbon on the earth [6]. Perturbations of hydrate stability and thawing of permafrost caused by ocean and atmospheric warming may lead to CH_4 being released into overlying sediments or water columns, which could exacerbate greenhouse warming. There is no conclusive evidence that hydrate-derived CH_4 is reaching the atmosphere now, but more observational data and improved numerical models will better characterize the climate-hydrate synergy in the future [7].

---

[*] Corresponding author at: Department of Geoscience and Engineering, TU Delft, Delft, Netherlands.
E-mail address: D.V.Voskov@tudelft.nl (D. Voskov).

https://doi.org/10.1016/j.ecmx.2026.101616
Received 8 December 2025; Received in revised form 13 January 2026; Accepted 22 January 2026

Nomenclature

Symbol	Definition
c	Component index $(1 \dots n_c)$
j	Phase index $(1 \dots n_p)$
ϕ	Porosity
ρ_j	Density of phase j
s_j	Saturation of phase j
x_{cj}	Mole fraction of component c in phase j
z_i	Overall mole fraction of component i
K	Absolute permeability tensor
k_{rj}	Relative permeability of phase j
μ_j	Viscosity of phase j
p	Pressure
T	Temperature
g	Gravitational acceleration
h_j	Specific enthalpy of phase j
U_j	Specific internal energy of phase j
κ	Thermal conductivity
$\Delta\psi_{lj}$	Phase–potential difference on interface l, phase j
υ_{ck}	Stoichiometric coefficient of component c in reaction k
r	Reaction rate
K_0	Kinetic pre-exponential constant
A_s	Hydrate reactive surface area
ΔE	Activation energy
f_w^H, f_w^k	Fugacity of water in hydrate and fluid phases
$S_{A,e}$	Effective aqueous saturation
$S_{G,e}$	Effective gas saturation
S^*	Scaled aqueous saturation
$S_{A,r}$, $S_{G,r}$	Residual saturations of aqueous and gas phases

From another perspective, naturally-occurring hydrate deposits are also recognized as a vast potential energy resource [8]. Recovery of natural gas from hydrate reservoirs relies on common production technologies such as depressurization, thermal stimulation, inhibitor injection and guest molecule exchange. The first three methods are aimed at destabilizing the hydrate by prohibiting hydrate formation conditions. The latter is rooted in the improved thermodynamic stability of a mixed hydrate phase over single-component hydrates and has the benefit of maintaining the structural integrity of the hydrate-bearing geological formation [9]. Furthermore, this process offers potential for carbon sequestration in hydrate deposits.

The interest in CO_2-hydrates, on the contrary, has primarily emerged from operational concerns in CO_2 sequestration [4]. Beyond operational risks, however, the formation of CO_2-hydrates in subsurface environments has attracted increasing attention as a promising pathway for long-term carbon storage. Hydrate-based CO_2 sequestration takes advantage of the fact that under sufficient pressure and low-temperature conditions, CO_2 can form thermodynamically stable hydrates in marine and permafrost sediments [10,11]. Compared to conventional supercritical CO_2 storage at higher temperatures and depths, hydrate-based storage offers additional safety through solid-phase trapping and reduced leakage potential [1,12]. Geological assessments have indicated that the hydrate stability zone (HSZ) in marine sediments can extend several hundred metres below the seafloor, providing a large volume for potential CO_2 immobilization [13].

Field data from geological surveys aimed at identifying the occurrence and properties of gas hydrate reservoirs have provided a wealth of information regarding CH_4-hydrates in porous media. Furthermore, several short-term field pilots have been carried out in permafrost- and marine hydrate deposits, such as the Ignik-Sikumi field trials at the Alaska North Slope [14]. These particular tests involved depressurization, as well as the guest molecule exchange of CH_4 with the injected CO_2-N_2 mixture.

However, controlling operating conditions in hydrate reservoirs is challenging due to complexity of interpretation of the field tests. Moreover, the dynamics of hydrate dissociation and formation, heat exchange due to the endothermic nature of hydrate phase behaviour and potential formation of ice upon hydrate production add to the operational complexities and have restricted short-termed field tests to typically days or weeks [15]. Therefore, numerical investigation of hydrate systems is essential to evaluate the production potential and develop strategies for the commercial use of hydrate reservoirs. This will lead to a better understanding and quantification of the dynamics of hydrate-bearing geologic media.

The majority of the existing literature on hydrates in porous media focuses on CH_4-hydrates. Historically, it has been the most common type of guest species, in oil and gas production and as a naturally occurring carbon source. As a consequence, the comparison and benchmarking of a numerical model for gas hydrates in porous media is limited to mostly single-component CH_4-hydrates. Nevertheless, single-component hydrates of CH_4 and CO_2 share a common thermodynamic basis. Therefore, only a few adjustments allow the use of the numerical model presented in this study for CO_2-hydrates as well. Besides, more lab experiments are performed to address hydrate formation issues in CO_2 sequestration operations [16,17].

Numerical studies on the simulation of gas hydrate systems in porous media are limited. The TOUGH+HYDRATE (T+H) simulator [18] is capable of simulating CH_4-hydrate formation and dissociation under kinetic and equilibrium conditions, involving the various production techniques destabilizing the hydrate. Other simulators that use a kinetic description of CH_4-hydrate formation and dissociation include CMG STARS [19] and MH21-HYDRES [20]. Furthermore, with the STOMP-HYDT-KE simulator [21], an attempt has been made to develop and demonstrate kinetic models representing the CH_4-CO_2-N_2 guest molecule exchange process that is presumed to have occurred during field tests [14]. More recently, the Full Implicit Simulator of Hydrate (FISH) has implemented a fully coupled thermal-hydraulic-chemical (THC) framework specifically for CO_2-hydrates and reproduces core-scale pressure, temperature, and hydrate-mass profiles within 10% deviation [22]. However, most models mentioned here assume that hydrate formation and dissociation are driven by a pressure difference relative to the hydrate equilibrium curve, rather than a thermodynamic (non-)equilibrium state. This assumption is limited to regions in the thermodynamic space where three phases (vapour-aqueous-hydrate) can coexist. Without excess water or with low gas concentrations, hydrate formation is still possible, but the required pressure can be above the equilibrium curve. Furthermore, the modelling of the hydrate phase equilibria under equilibrium assumptions in T+H is based on tabulated equilibrium constants [23].

In this study, we extend the in-house open-DARTS simulation framework [24], which is capable of modelling complex flow and transport related to various energy applications and CO_2 sequestration [25–28]. We utilize a thermal-compositional-reactive formulation [29] to implement a full thermodynamic description of CH_4- and CO_2-hydrate formation and dissociation in porous media under kinetic assumptions. The complexity of such systems can be effectively captured using the Operator-Based Linearization (OBL) approach. The OBL method significantly simplifies the implementation of a complex simulation framework by introducing algebraic functions that capture all complex physics and associated nonlinear terms. It provides an opportunity to represent the exact physics of the simulation problem by operators defined at each point in the discrete parameter space from the set of primary unknowns. The main advantage of this approach is a simplified construction of the Jacobian matrix and residuals since the complex physics-based calculations (i.e., mainly related to the flux in the governing equations) are translated into algebraic multi-linear interpolation kernels [25]. The method enables the combination of conventional conservation equations with the use of complex physics and empirical models.

This paper is structured as follows. First, we briefly describe our numerical model and the Operator-Based Linearization approach. Next, we develop the workflow for thermodynamic calculations for hydrate systems under kinetic assumptions. We analyse the Gibbs energy surfaces of each of the fluid and hydrate phases to confirm that, in the limit, kinetic assumptions would yield the same conditions as equilibrium thermodynamics. Finally, we benchmark the simulation model for CH_4- and CO_2-hydrate formation and dissociation against numerical benchmarks from literature using several test cases [8,22,30]. A convergence study is included to validate the use of the OBL approach.

2. Numerical methodology

In this section, we are going to formulate governing equations, outline the impact of hydrates on flow and introduce an operator-based linearization approach for an accurate and flexible treatment of nonlinearity.

2.1. Conservation of mass and energy

For a domain with volume Ω, bounded by surface Γ, the conservation of mass and energy can be expressed in a uniformly integral way, as

$$\frac{\partial}{\partial t}\int_{\Omega} M^c d\Omega + \int_{\Gamma} \boldsymbol{F}^c \cdot \boldsymbol{n} d\Gamma = \int_{\Omega} Q^c d\Omega \tag{1}$$

Here, M^c denotes the accumulation term for the cth component ($c = 1, \dots, n_c$, indexing for the mass components and $c = n_c + 1$ for the energy quantity); $\boldsymbol{F}_c$ refers to the flux term of the cth component; $\boldsymbol{n}$ refers to the unit normal pointing outward to the domain boundary; Q_c denotes the source/sink term of the cth component.

In this work, fluid flow is governed by advective and diffusive fluxes, and the source term contains source/sink terms for wells and kinetic reactions. The energy accumulation term contains both the fluids and rock, and the flux term for energy accounts for advection and conduction. For each component c, the mass conservation equation can be expressed as

$$\frac{\partial}{\partial t}\Big(\phi \sum_{j=1}^{n_p} \rho_j s_j x_{cj}\Big) = -\nabla \cdot \Big(\sum_{j=1}^{n_p} x_{cj}\rho_j \boldsymbol{u}_j + s_j \rho_j \mathbf{J}_{cj}\Big) + \sum_{j=1}^{n_p} x_{cj}\rho_{mj} q_j + \sum_{k=1}^{n_k} v_{ck} r_k \quad c = 1, \dots, n_c \tag{2}$$

and for energy

$$\frac{\partial}{\partial t}\Big(\phi \sum_{j=1}^{n_p} \rho_j s_j U_j + (1-\phi)U_r\Big) = -\nabla \cdot \Big(\sum_{j=1}^{n_p} h_j \rho_j \boldsymbol{u}_j + \kappa \nabla T\Big) + \sum_{j=1}^{n_p} h_j \rho_j \hat{q}_j \tag{3}$$

Here, the velocity $\boldsymbol{u}_j$ follows the extension of Darcy's law for multiphase flow:

$$\boldsymbol{u}_j = -\mathbf{K}\frac{k_{rj}}{\mu_j}(\nabla p_j - \boldsymbol{\gamma}_j \nabla z), \tag{4}$$

which includes gravitational and capillary effects. The diffusive flux $\mathbf{J}_{cj}$ of component c in phase j is described by Fick's law as

$$\mathbf{J}_{cj} = -\phi \mathbf{D}_{cj} \nabla x_{cj}, \tag{5}$$

The rock is assumed compressible and represented by the change of porosity through

$$\phi = \phi_0\big(1 + c_r(p - p_{ref})\big) \tag{6}$$

The nonlinear equations are discretized using finite-volume discretization with a two-point flux approximation and upstream weighting [31] in space and a backward Euler approximation in time. The discretized residual form for a reservoir block i bounded by interfaces l reads

$$R_i^c = V_i\Big(M_i^c(\omega_i) - M_i^c(\omega_i^n)\Big) - \Delta t\Big(\sum_l A_l F_l^c(\omega) + V_i Q_i^c(\omega)\Big) = 0, \quad c = 1, \dots, n_c + 1. \tag{7}$$

2.2. Operator form of conservation equations

The nonlinearity of the system of mass and energy conservation equations, introduced by the secondary variables that depend on the values of nonlinear unknowns at the current time-step, is further increased by the assumption of instantaneous thermodynamic equilibrium, which requires a multiphase flash procedure for each grid block.

The operator-based linearization approach [32] significantly simplifies the implementation of complex simulation frameworks by introducing algebraic operators that capture all complex physics and nonlinear terms. Instead of keeping track of each property and its derivatives with respect to nonlinear unknowns, abstract algebraic operators representing the physics can be constructed and assembled into the set of Jacobian and residuals defined at each iteration.

In the described approximation method, pressure, temperature and overall composition are taken as the unified state variables in a given control volume. Upstream weighting of the physical state is used to determine the flux-related fluid properties determined at the interface l. The discretized mass conservation equation in operator form for each grid block reads

$$V\phi_0[\alpha_c(\omega) - \alpha_c(\omega_n)] - \Delta t \sum_{l\in L(i)} \sum_{j=1}^{n_p} \big[\Gamma^l \beta_{cj}^l(\omega^u)\Delta\psi_j^l + \Gamma_d^l \gamma_j^l(\omega)\Delta\chi_{cj}\big] + \Delta t V \delta_c(\omega) = 0, \quad c = 1, \dots, n_c \tag{8}$$

Here we define the following state-dependent operators,

$$\alpha_{cf}(\omega) = \Big(1 + c_r(p - p_{ref})\Big)\sum_{j=1}^{n_p} x_{cj}\rho_j s_j, \ c = 1, \dots, n_c; \tag{9}$$

$$\beta_{cj}(\omega) = x_{cj}\rho_j k_{rj}/\mu_j, \ c = 1, \dots, n_c, \ j = 1, \dots, n_p; \tag{10}$$

$$\gamma_j(\omega) = \Big(1 + c_r(p - p_{ref})\Big)\rho_j s_j, \ j = 1, \dots, n_p; \tag{11}$$

$$\chi_{cj}(\omega) = D_{cj} x_{cj}, \ c = 1, \dots, n_c, \ j = 1, \dots, n_p; \tag{12}$$

$$\delta_c(\omega) = \sum_{j=1}^{n_p} v_{cj} r_j(\omega), \ c = 1, \dots, n_c. \tag{13}$$

The phase-potential-upwinding (PPU) strategy for OBL parametrization is applied to model the gravity and capillary effect [25,33]. The potential difference of phase j on the interface l between block 1 and 2 can be written as:

$$\Delta\psi_j^l = p_1 - p_j^c(\omega_1) - (p_2 - p_j^c(\omega_2)) - \frac{\rho_j(\omega_1) + \rho_j(\omega_2)}{2} g(z_2 - z_1), \tag{14}$$

where p_j^c is the capillary pressure.

The discretized energy conservation equation in operator form can be written as:

$$\begin{aligned} &V\phi_0[\alpha_{ef}(\omega) - \alpha_{ef}(\omega_n)] - \Delta t \sum_{l\in L(i)} \sum_{j=1}^{n_p} [\Gamma^l \beta_{ej}^l(\omega^u)\Delta\psi_j^l + \Gamma_d^l \gamma_j(\omega)\Delta\chi_{ej}] \\ &\quad + \Delta t V \delta_e(\omega) + (1-\phi_0)V U_r[\alpha_{er}(\omega) - \alpha_{er}(\omega_n)] \\ &\quad - \Delta t \sum_l (1-\phi_0)\Gamma_d^l \kappa_r \alpha_{er}(\omega)\Delta\chi_{er} = 0, \end{aligned} \tag{15}$$

where:

$$\alpha_{ef}(\omega) = \Big(1 + c_r(p - p_{ref})\Big)\sum_{j=1}^{n_p} \rho_j s_j U_j; \tag{16}$$

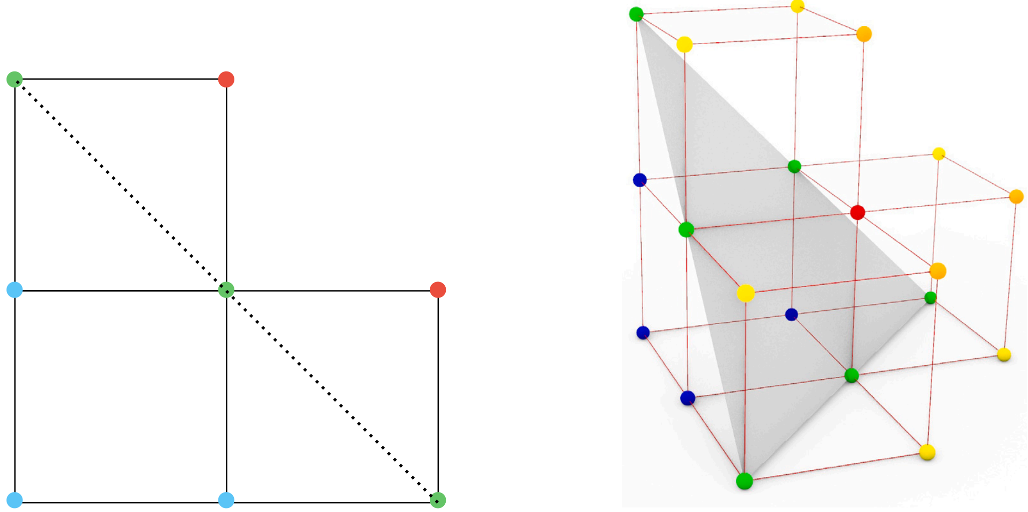

(a) Three-component space

(b) Four-component space

Fig. 1. Hypercubes in multicomponent compositional space. (For interpretation of the references to colour in this figure legend, the reader is referred to the web version of this article.)

$$\beta_{ej}(\omega) = h_j \rho_j k_{rj}/\mu_j, \; j = 1, \ldots, n_p; \tag{17}$$

$$\chi_{ej}(\omega) = \kappa_j T_j, \; j = 1, \ldots, n_p; \tag{18}$$

$$\delta_e(\omega) = \sum_{j=1}^{n_j} v_{ej} r_{ej}(\omega) \tag{19}$$

In this form, the nonlinear system is defined only in terms of physical state-dependent operators. The values of these operators are uniquely determined in the parameter space of the simulation problem with the set of primary unknowns $\{P, T, z_1, \ldots, z_{n_c-1}\}$. Approximation interpolants are generated at each point in the discrete parameter space at the pre-processing stage and stored in $(n_c + 1)$-dimensional tables. The approach was modified [25] to adaptively evaluate the operators during simulation, improving the overall performance of the solution. Operator values for a specific state are obtained by multilinear interpolation of tabulated values. Partial derivatives, required for the assembly of the Jacobian matrix, can be evaluated directly as interpolation coefficients. However, to delineate the nonlinear behaviour in the system, especially strong nonlinearity, it is necessary to select a reasonable OBL resolution to characterize the physical space. Too coarse OBL resolution may lead to large errors in the solutions [32].

2.3. A note on OBL parametrization for multicomponent systems

In multicomponent systems, a multilinear interpolation strategy for OBL may require evaluation of supporting points for which the composition of the last component is negative. This is the case for compositions that are located in an interpolation hypercube that is intersected by the edge of the compositional space where $z_{n_c} = 0$. For these compositions, one supporting point corresponds to a coordinate where the $n_c - 1$ independent mole fractions sum up to a value greater than unity. Such a state is non-physical, and therefore a different approach must be used to evaluate operator values at these supporting points.

Fig. 1 shows how the $(n_c - 1)$-dimensional compositional domain of the OBL discretization at the edge of the physical parameter space for (a) three- and (b) four-component simulations. In the hypercubes that are intersected by $z_{n_c} = 0$, some of the supporting points correspond to $z_{n_c} > 0$ (blue), some are located exactly on the edge (green) and a few lie outside of the physical space (red, orange, yellow). A solution to obtain consistent values for interpolation lies in the linear nature of the parameter space within each hypercube. Using this property, the OBL implementation for these hypercubes requires extrapolation of the operator values in the physical coordinates to calculate the corresponding operator values in the non-physical supporting point.

Mathematically, this is described as a hyperplane that goes through the physical supporting points. In the (n_c-1)-dimensional compositional subspace with the additional dimension of operator value, this corresponds to the set of points $\mathbf{y} = (x_1, \ldots, x_N)$ in $\mathbb{R}^N$ with $N = n_c$. The equation for a hyperplane in $\mathbb{R}^N$ through point $\mathbf{p}$ with normal vector $\mathbf{n}$ is given by

$$\sum_n^N a_n (y_n - p_n) = 0 \tag{20}$$

or

$$\sum_n^N a_n y_n = -d \tag{21}$$

where $d = -\mathbf{n} \cdot \mathbf{p}$.

One can extrapolate the operator values at the physical points to the non-physical coordinate by determining the equation of the hyperplane. This can be done by finding the null vector $\mathbf{h}$ of matrix $\mathbf{P}$ that contains the coordinates of the N known coordinates $\mathbf{p}_N$ and operator values α_N:

$$\begin{pmatrix} z_{11} & \ldots & z_{1,n_c-1} & \alpha_1 & 1 \\ \vdots & \ddots & & & \\ z_{N1} & \ldots & z_{N,n_c-1} & \alpha_N & 1 \end{pmatrix} \tag{22}$$

After performing a Gaussian elimination of the matrix (22), the extrapolated operator value can be found by substituting the non-physical coordinate into the obtained equation of the hyperplane.

By definition of the linear nature of the hyperplane, interpolated values at the edge of the physical domain are linearly interpolated between the supporting points that correspond to $z_{n_c} = 0$. As a result, any interpolated states at a composition with $z_{n_c} = 0$ that should be zero by being located at the edge of the composition domain, are indeed zero.

For the three-component problem (Fig. 1a), extrapolation always occurs in the three-dimensional subspace. In the four-component space (and up), however, more varieties of cases exists. In case all $n_c - 1$ compositions are nonzero, the extrapolation relies on a different set

Table 1

Flow behaviour models used in this study (normalization/effective saturations, capillary pressure, and relative permeability).

Property	CH_4-hydrate formation [8]	CO_2-hydrate formation [22]	CH_4-hydrate dissociation (cases A & B) [30]
Effective saturations	$S_{A,e} = \frac{S_A}{S_A + S_G}$, $S_{G,e} = \frac{S_G}{S_A + S_G}$, $S^* = \frac{S_A - S_{A,r}}{S_{A,\max} - S_{A,r}}$ *used in all studies*		
Capillary pressure	$P_c = -P_0\left[(S^*)^{-1/\lambda} - 1\right]^{-\lambda}$ $P_0 = 2000$ Pa, $\lambda = 0.6$, $S_{A,r} = 0.12, \quad S_{A,max} = 1$	$P_c = P_0\left(\frac{S_{A,e} - S_{A,r,e}}{1 - S_{A,r,e}}\right)^{-n_{\mathrm{cap}}}$ $P_0 = 1000$ Pa, $n_{\mathrm{cap}} = 1.00$ $S_{A,r} = 0.10$	*Same relation as CH_4-hydrate formation case was used* Case A: $P_0 = 1887.0$ Pa, $\lambda = 0.60$, $S_{A,r} = 0.12, \quad S_{A,\max} = 1.0$ Case B: $P_0 = 12500$ Pa, $\lambda = 0.45$, $S_{A,r} = 0.12, \quad S_{A,\max} = 1.0$
Relative permeability	$k_{rA} = k_{rA,0}\left(\frac{S_{A,e} - S_{A,r,e}}{1 - S_{A,r,e}}\right)^{n_A}$, $k_{rG} = k_{rG,0}\left(\frac{S_{G,e} - S_{G,r,e}}{1 - S_{A,r,e}}\right)^{n_G}$ $k_{rA,0} = k_{rG,0} = 1, \quad n_A = n_G = 3$ $S_{A,r} = 0.12, \quad S_{G,r} = 0.02$	*Same relation as CH_4-hydrate formation case was used* $k_{rA,0} = k_{rG,0} = 1, \quad n_A = n_G = 3$ $S_{A,r} = 0.10, \quad S_{G,r} = 0.05$	*Same relation and parameter as CH_4-hydrate formation case were used*

of supporting points in the red and orange states (Fig. 1b). If the extrapolation concerns a state where one or more of the compositions are zero, one of the axes degenerates and the problem reduces to $n_c - 1$ dimensional extrapolation (yellow).

2.4. Impact of hydrates on flow behaviour

This section describes the constitutive laws that couple hydrate saturation to multiphase flow and transport. Specifically, we define the effective pore volume and the corresponding saturation normalization used for mobilities, state the relative-permeability relations, specify the capillary-pressure relation, and prescribe the reduction of absolute permeability with hydrate saturation evolution. These choices are consistent with established hydrate simulators and benchmarks [8,22,30] and with our OBL implementation, where the same forms are applied and parameters and relations are reported per case in Table 1.

- **Normalization/effective saturations:** Hydrate is treated as an immobile solid that occupies a fraction S_H of pore space, leaving $(1 - S_H)$ for the mobile fluids. For capillary and relative permeability models we therefore use effective saturation.
- **Capillary pressure:** We define gas/water capillary pressure with a van Genuchten form [34], where P_0 is the entry pressure and n_{cap} and λ are exponents in capillary pressure model. The sign of the capillary pressure should be defined based on the reference phase of the simulator.
- **Relative permeability:** Phase mobilities follow Corey curves in effective saturation: with $S_{A,e}$ from effective properties.
- **Absolute permeability reduction:**Absolute permeability decreases as the hydrate fills the pore space. In Tough+Hydrate simulator, the first evolving porous medium (EPM) model from [23] and for CO_2-hydrate formation case from Reference [22], the model is as follows:

$$k = k_0\left(1 - S_H\right)^{n+2}\left(\frac{A_0}{A_H}\right)^2, \qquad n = 3, \tag{23}$$

With a geometric factor A_0/A_H. For small hydrate saturation, the pore cross-sectional area scales as

$$\frac{A_0}{A_H} = \left(1 + \sqrt{S_H}\right)^{-1}, \qquad S_H < 0.10, \tag{24}$$

For larger hydrate saturation $(0.10 \le S_H)$, let $x = r/L \in [1, \sqrt{2}]$ be the normalized throat radius, linked to S_H by:

$$1 - S_H = \frac{-\frac{\pi}{3}x^3 + \frac{3\pi}{4}x^2 - \frac{5\pi}{12}x + \frac{\pi}{6}}{1 - \frac{\pi}{6}}, \qquad x \in [1, \sqrt{2}], \tag{25}$$

and the corresponding area ratio

$$\frac{A_0}{A_H} = \frac{3\sqrt{2} - 4}{3x - 2x^2} \tag{26}$$

Eqs. (23)–(26) recover $k \to k_0$ as $S_H \to 0$ and yield a monotone decrease with S_H.

In this work, we adopt the permeability model, consistent with the benchmark problems used in Section 4. The goal of these sections is to reproduce and validate published CH_4 and CO_2-hydrate studies under the same modelling assumptions, rather than to compare alternative permeability relationships. The OBL framework itself is independent of the particular permeability model and other relations (e.g. Kozeny–Carman or Tokyo-type correlations) could be substituted without changing the numerical formulation.

3. Thermodynamic description of hydrate systems

Hydrates can form in any system that contain water and the presence of small, non-polar guest molecules, either undersaturated in aqueous solution or as a free phase. The hydrate pseudo-reaction is given by:

$$\mathrm{G} + \mathrm{n_H H_2O} \longleftrightarrow \mathrm{G \cdot n_H H_2O} \tag{27}$$

The hydration number $\mathrm{n_H}$ corresponds to the number of water molecules bound to each guest molecule G. Hydrates are non-stoichiometric substances, i.e., they have no set chemical composition.

Full cage occupancy of sI-hydrate corresponds to 8 guest molecules per 46 H_2O molecules and would yield a hydration number of 5.75. In reality, full cage occupancy is not a thermodynamically favourable state and the composition of the hydrate phase varies with thermodynamic conditions.

The conditions for hydrates to exist then require rather low temperatures, though not necessarily sub-zero, and sufficiently high pressures. However, formation conditions, (non-stoichiometric) composition, and structure type (sI, sII, sH) of hydrates are highly dependent on fluid composition. As a result, mixed guest hydrates introduce a very nonlinear thermodynamic behaviour which cannot be easily understood without considering a full thermodynamic equilibrium approach including hydrate phases.

For single-guest hydrates, such as nearly-pure CH_4-hydrates in natural hydrate deposits or natural gas pipelines or CO_2-hydrates in carbon sequestration operations, a thermodynamic model using a kinetic description for the hydrate phase is, in many cases, a better approximation of the dynamics. This holds especially for hydrate systems in porous media, where nucleation highly depends on local conditions and pore-scale geometry limits transport of matter to the hydrate surface and governs the ability to sustain the growth process [30].

In this work, we limit ourselves to a two-component system containing H_2O and CH_4 or CO_2, which are limited to partition into non-aqueous (V/L), aqueous (Aq) or sI-hydrate (H) phases. We discuss the thermodynamic model for single-component CH_4 and CO_2-hydrates. According to Gibbs' phase rule, the degrees of freedom at equilibrium amount to $F = C - P + 2$. This implies that a three-phase equilibrium can only occur at the phase boundary (the hydrate equilibrium curve), where pressure (or temperature) behaves as a dependent variable. By means of a Gibbs energy analysis, we demonstrate that both kinetic and equilibrium approaches yield the same equilibrated conditions given enough time. In the mass balance equations (2), however, the hydration number is often fixed. An aspect that is not easily captured using a kinetic model with a set hydrate composition is the variability in gas 'stoichiometry' throughout the equilibration process. This phenomenon is relatively harmless for single-component hydrates, but becomes crucial for modelling of mixed hydrates [35].

3.1. Thermodynamic description of kinetic model

A kinetic description of the hydrate phase requires a flash procedure for solving thermodynamic equilibrium only between the fluid phases. The assumption of instantaneous thermodynamic equilibrium is not applied to the hydrate phase, and a separate mass balance equation for the hydrate pseudo-component is added. The kinetic pseudo-reaction of the hydrate phase is then driven by the difference in fugacities of water between fluid and hydrate phases:

$$r_k \propto \Delta f_w \tag{28}$$

The process of formation or dissociation results in a net exchange of mass between hydrate and non-hydrate phases to minimize Gibbs energy and restore thermodynamic equilibrium between all phases. The complete set of rate laws described by modified Arrhenius-type relations is used for the simulation scenarios and accompanied by the Results section (Table 2).

The proposed thermodynamic framework for kinetics consists of two stages. Firstly, a two-phase flash procedure yields the thermodynamic equilibrium between the fluid phases. Secondly, the hydrate reaction rate is determined from the fugacity difference between the fluid and hydrate phases. We demonstrate that the conditions of the equilibrated system obtained with kinetic assumptions are, in the limit, equivalent to those obtained from equilibrium assumptions.

3.2. Flash procedure for fluid phases

At thermodynamic equilibrium, pressure and temperature are uniform throughout the system. Furthermore, the Gibbs free energy of an equilibrium mixture is at a global minimum. The Gibbs free energy is given by:

$$\overline{G} = G/RT = \sum_{k=1}^{n_p} \sum_{i=1}^{n_c} n_{ik} \ln f_{ik} \tag{29}$$

with n_{ik} and f_{ik} the number of moles and fugacity of species i in phase k, respectively. At the global minimum, the change in Gibbs energy for any transfer of material must be zero:

$$\frac{\partial \overline{G}}{\partial n_{ik}} = \ln f_{ik} - \ln f_{iR} = 0, \quad i = 1, \dots, n_c; k = 1, \dots, n_p; k \neq R, \tag{30}$$

where the reference phase R can be any phase. Hence, this yields the equality of fugacity of each component i throughout all phases k as a necessary condition for equilibrium.

Since it is generally not known in advance how many phases coexist at a global minimum, a sequence of phase stability and split routines must commonly be performed to find the correct equilibrium state. The stability test and phase split problems have similar mathematical structures. In a recent work [36], we adapted the procedures described by Reference [37,38] for hybrid models. A stability test indicates whether the Gibbs energy surface is either at or above the mixture tangent hyperplane throughout the entire compositional space [39,40]. Reference [41] developed a mathematical implementation of this "tangent plane distance" (TPD) criterion. The common approach to finding the minima of the TPD function is to apply local optimization over a set of initial guesses. The corresponding phase compositions can be used as an initial estimate in further phase split calculations.

In the phase split procedure, the dimensionless Gibbs energy (29) is minimized with respect to mole numbers. In addition, in SSI iterations or if lnK are used as independent variables in the Newton method, the material balance must be satisfied, generally done so by solving the Rachford-Rice (RR) system of equations:

$$R_k \equiv \sum_{i=1}^{n_c} (x_{ik} - x_{iR}) = \sum_{i=1}^{n_c} \frac{z_i (K_{ik} - 1)}{1 + \sum_{p=1}^{n_p} \theta_p (K_{ip} - 1)} = 0, \quad k = 1, \dots, n_p; k \neq R. \tag{31}$$

The equilibrium constants K_{ik} describe the mole fraction ratio of each component between phase k and the reference phase. The solution to the RR equations yields the phase fractions $\boldsymbol{\theta} = (\theta_1, \dots, \theta_k)^T$ and phase compositions $\mathbf{x}_k$. For two phases, the RR equation can be solved using convex transformations, as proposed by Reference [42], leading to a significant increase in solution speed in difficult cases.

3.3. Thermodynamic models and hybrid-EoS approach

Cubic equations of state have proven reliable for thermodynamic calculations of nonpolar mixtures, but are not adequate to predict the interaction between associating particles in aqueous solutions. Besides, they fail to describe the behaviour close to infinite dilution. For the fluid phases, we rely on the recently proposed hybrid-EoS framework with a fugacity-activity model for the aqueous phase and cubic EoS for non-aqueous fluid phases [36].

The implementation of a separate model for the aqueous phase maintains the simplicity of solving phase equilibrium problems with cubic equations of state while obtaining an accurate thermodynamic description of the aqueous phase. For the aqueous model, we combine activity coefficient models based on Henry's law constants for the dissolved species [43,44] and a separate fugacity model for the H_2O component [45] to calculate the aqueous phase fugacities. An accurate evaluation of aqueous phase properties is particularly important for hydrate modelling, where gas solubility and component fugacities have

Table 2
Summary of hydrate formation/dissociation kinetic models and parameters employed in numerical studies.

Study	Kinetic model and parameters	A_s/geometric term
CH_4-hydrate formation [8]	$r = K_{f0} A_s \exp\left(-\frac{E_a}{RT}\right)(f_w^H - f_w^k)$ $K_{f0} = 3.6 \times 10^4 \ \mathrm{mol\,Pa^{-1}\,m^{-2}\,s^{-1}}$ $E_a = 8.1 \times 10^4 \ \mathrm{J\,mol^{-1}}$ $n_H = 6.1$ $R = 8.314 \ \mathrm{J\,mol^{-1}\,K^{-1}}$	$A_s = 0.879\, F_A(t)\, \frac{1-\phi}{r_p}\, S_H^{2/3}$ $r_p = \left[\frac{45\,k}{(1-\phi)^2\,\phi^3}\right]^{1/2}$ $F_A = 0.23$
CH_4-hydrate dissociation [30]	$r = K_{d0} A_s \exp\left(-\frac{E_a}{RT}\right)(f_w^H - f_w^k)$ $K_{d0} = 3.6 \times 10^4 \ \mathrm{kg\,Pa^{-1}\,m^{-2}\,s^{-1}}$ $E_a = 8.1 \times 10^4 \ \mathrm{J\,mol^{-1}}$ $n_H = 6.1$	A_s and r_p same as CH_4-hydrate formation study $F_A = 1.0$
CO_2-hydrate formation [22]	$r = 3K_{f0} \exp\left(-\frac{E_a}{RT}\right) S_A^{\beta}(1 - S_H)^{\beta}\, \frac{1-\phi}{r_p}\, S_G^{2/3}(f_w^H - f_w^k)$ $K_{f0} = 8.4 \times 10^{11} \ \mathrm{kg\,m^{-2}\,Pa^{-1}\,s^{-1}}$ $E_a = 1.0288 \times 10^5 \ \mathrm{J\,mol^{-1}}$ $\beta = 5.3$ $n_H = 6.0$	No separate A_s; geometric factor is inside the rate. $r_p = 1.645 \times 10^{-4}$ m

a large influence on the predicted hydrate equilibria [46]. Considering the limited solubility of gases in the aqueous phase, the use of Henry's law coefficients is valid.

The hybrid-model approach introduces a thermodynamic inconsistency that is mostly pronounced close to critical conditions. Far from brine criticality, however, robust, accurate and efficient solution procedures are obtained. In practice, hydrate calculations are limited to a narrow range of temperature and a wide range of pressure and the use of inconsistencies towards critical conditions of the brine phase by using separate equations of state are therefore not a concern [45].

It must furthermore be noted that, albeit the Peng–Robinson EoS [47] is often preferred because of improved (critical) compressibility factors, predictions of hydrate structures and equilibrium pressures obtained with the Soave–Redlich–Kwong EoS [48] are more satisfactory. This is due to the fact that the improvement in volumes is at the expense of the (critical) fugacity coefficient [46]. In the reference studies that we aim to reproduce in this work, however, the Peng–Robinson EoS is utilized.

To calculate hydrate fugacity and determine the magnitude of the thermodynamic driving force (28), the common procedure in the literature relates to the hydrate equilibrium curve. In this work, however, we evaluate the fugacity of water in the hydrate phase from a modified Van der Waals–Platteeuw hydrate equation of state [49,50] (Appendix A)

3.4. Gibbs energy analysis of kinetic assumptions

Contrary to equilibrium assumptions, where the hydrate phase is incorporated into a multiphase flash procedure, the kinetic model assumes a thermodynamic non-equilibrium between the fluid and hydrate phases. In the limit, however, both tend to the direction of minimum Gibbs energy. We demonstrate this by analysing the Gibbs energy surfaces of the three phases.

Fig. 2 shows the dimensionless Gibbs energy of mixing surfaces for the H_2O-CH_4 system at a temperature of 277.6 K, typically encountered at the sea floor [51]. Note that the surfaces of the fluid phases are only plotted for relevant ranges of composition (i.e., CH_4-rich for the vapour phase, H_2O-rich for the aqueous phase). The composition of the hydrate phase, however, is physically limited to the range between empty ($z_{H_2O} = 1$) and full cage occupancy ($z_{H_2O} \approx 0.85$).

The fugacity of each separate component can be calculated from its intersection with the y-axis at pure composition. The guest molecule fugacity is taken from the fluid-phase equilibrium. The stability of hydrate at specified conditions is indicated by whether the hydrate fugacity is above or below fluid-phase equilibrium.

Three different pressures are considered: below hydrate equilibrium pressure (P = 10.0 bar), exactly at the three-phase coexistence curve (P = 40.79 bar) and above hydrate equilibrium pressure (P = 70.0 bar). At thermodynamic equilibrium between any number of phases, the chemical potential of each component is equal throughout all equilibrium phases. In the Gibbs energy diagram, this corresponds to a common tangent to the surface at each of the equilibrium phase compositions. It can be observed that the Gibbs energy surface of the hydrate phase for the three pressures is above, exactly at and below the Gibbs energy surface for two-phase equilibrium, respectively.

Using the fugacity of CH_4 in the fluid phases to calculate the hydrate fugacity, the tangent to the hydrate surface indicates that total Gibbs energy would be decreased by either hydrate formation ($P > P_{eq} : f_k > f_H$) or dissociation ($P < P_{eq} : f_k < f_H$). Through the consumption or release of gas upon formation or dissociation, respectively, the system decreases or increases its pressure accordingly to return to equilibrium.

From the Gibbs energy analysis, we find that, as was implied by Gibbs' phase rule, three-phase equilibrium in a binary system occurs only at the phase boundary between the three phases, which corresponds to the hydrate equilibrium curve. In single-phase fluid conditions – either when the brine is undersaturated with dissolved CH_4, or all water is evaporated – we would find that increasingly large pressures are necessary to sustain a stable hydrate phase.

Aside from finding equilibrium conditions of the hydrate phase, note that the phase equilibrium conditions also determine the composition of the hydrate phase. It corresponds to the tangent line to the hydrate surface, which varies from low cage occupancy in brine-hydrate conditions to high concentrations of CH_4 in the vapour-hydrate region.

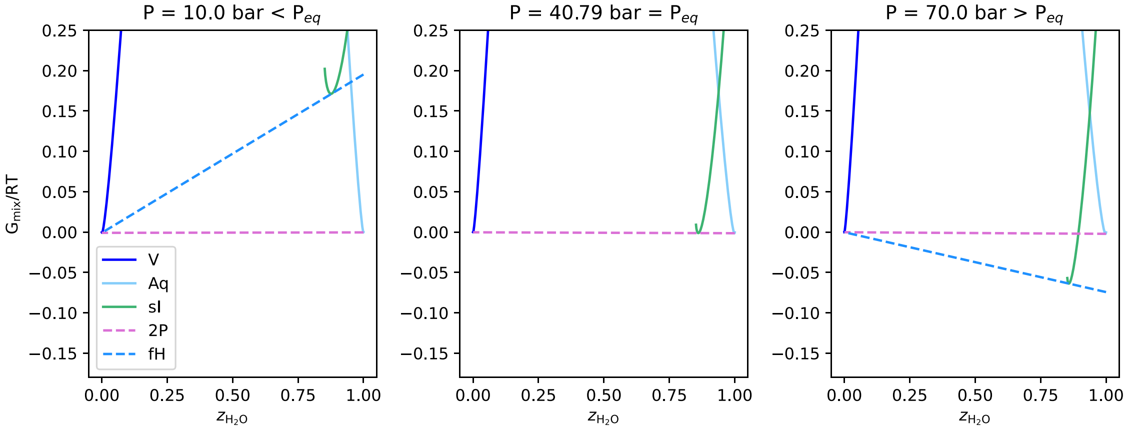

Fig. 2. Gibbs energy surfaces of mixing of H_2O-CH_4 mixture at $T = 277.6$ K for conditions below equilibrium pressure (P = 10.0 bar), at the three-phase boundary (P = 40.79 bar) and above equilibrium pressure (P = 70.0 bar). The solid lines are the Gibbs energy of mixing surfaces for hypothetical single-phase mixtures and the dashed lines are the Gibbs energy of mixing of two-phase equilibrium, and of the hydrate phase at the given two-phase equilibrium.

Table 3
Reactor and porous medium properties for formation experiments.

Parameter	CH_4	CO_2
Internal height of reactor	120.0 mm	160.0 mm
Internal diameter of reactor	102.0 mm	101.6 mm
Internal volume of reactor	0.98 L	1.155 L
External height of reactor	170.0 mm	164.0 mm
External diameter of reactor	132.0 mm	116.0 mm
Thickness of reactor wall	15 mm	7.2 mm
Material of reactor	SS316 steel	Steel
Radius sensor a	25.0 mm	N.A.
Radius sensor b	38.0 mm	N.A.
Porosity ϕ	0.44	0.312
Permeability k	3.83 D	30.0 D
Density of rock ρ_r	2650 kg/m^3	2075.5 kg/m^3
Thermal conductivity of dry rock κ_d	0.30 W/m K	2.2 W/m K
Thermal conductivity of wet rock κ_w	1.65 W/m K	N.A.
Heat capacity of rock $c_{p,r}$	1400 J/kg K	745 J/kg K
Thermal conductivity of Steel κ_s	16.0 W/m K	13.4 W/m K
Heat capacity of Steel $c_{p,s}$	500 J/kg K	468 J/kg K

4. Results

In this section, we apply the modelling framework to simulate gas hydrates in porous media. We first reproduce hydrate formation the numerical experiments for CH_4 [8] and CO_2 [22]. Then, we investigate test cases for dissociation of natural CH_4-hydrate deposits as studied by Reference [30]. The reaction models for each case have been summarized in Table 2. Note that we adopt the same kinetic rate parameters, porosity-permeability relationships, spatial grids and boundary conditions as in the original publications, since the primary goal here is to reproduce and validate the reported behaviour.

4.1. Hydrates formation

Authors of Reference [8,52] analysed numerically earlier experimental studies that involved CH_4-hydrate formation and dissociation in a small reactor filled with a sandy porous medium. Their study aimed to investigate the hydrate reaction kinetics and phase distribution heterogeneity throughout core samples in such laboratory studies. In line with the setup for CH_4-hydrates, we simulate a CO_2-hydrate formation experiment under a semi-batch, constant-pressure configuration [22]. The core properties for both experiments are summarized in Table 3.

4.1.1. CH_4 – hydrate formation

The CH_4-hydrate formation experiment describes a 1.0L cylindrical reactor, blanketed by a cooling jacket that circulates a heat exchange fluid. A stainless-steel wall surrounds the porous medium and is used for cooling via the external bath; in the model, the wall is treated as a solid, impermeable layer with zero porosity (no mass flow through the wall). A water injection point is located at the top of the reactor. Pressure sensors record pressure at the top and bottom, and thermal sensors T_a and T_b are installed at different radii throughout the core. The core is initially pressurized by pure CH_4. Then, three sequences of water injection (I), stabilization (S), and hydrate formation (F) stages followed, allowing the system to return to equilibrium.

We model the first stage of hydrate formation $F1$. The bath temperature and pressure initially measure 288.2 K and 95.0 bar and are practically uniform. The cooling fluid starts circulating the boundary, its temperature slowly reduced to 274.5 K (reached at $t = 0.66$ hr). The temperature at the boundaries is maintained constant for the remainder of 24 h. This is sufficiently low to create hydrate formation conditions. The rate of hydrate formation is described in Table 2.

Fig. 3 shows the temporal and spatial evolution of pressure (a), temperature (c) and phase distributions (e). The high porosity and permeability of the sand result in a practically uniform pressure distribution at all times. The temperature distribution is heterogeneous at early times, caused by the combined effect of the cooling boundary and the exothermic nature of hydrate formation. The temperature drop at the boundary spreads into the core by means of thermal conduction, then increases due to the heat released upon hydrate formation and becomes uniform after 4 h. A similar heterogeneous distribution of hydrates to Reference [8] can be observed. They recorded a hydrate saturation of 0.49 at the cooling boundary and a saturation of only 0.10 at the centre of the core. In our simulations, the distributions are slightly different. Notice that the pattern of hydrate distribution heavily depends on the kinetic parameters and thermal properties of the medium.

Under hydrate-forming conditions, the system pressure and temperature gradually decrease as the boundary cools. The pressure–temperature trajectories at sensors A and B (Fig. 4) show that both locations follow a cooling path that progressively departs from the equilibrium curve as hydrates begin to form. The deviation below the equilibrium line indicates the consumption of free gas and water for hydrate generation, while the subsequent pressure stabilization reflects the slowing of formation as the system approaches equilibrium.

4.1.2. CO_2 – hydrate formation

We reproduce the semi-batch/constant-pressure configuration (run 3) of the CO_2-hydrate formation experiment reported by Reference [22]. Initial conditions correspond to a uniform $T = 1.95\,°\mathrm{C}$ and $P = 3.20\,\mathrm{MPa}$. In the sand bed, $S_A = 0.25$, $S_G = 0.75$. The gas cap is void ($\phi = 0.99$) that is saturated with nearly pure CO_2. All steel walls

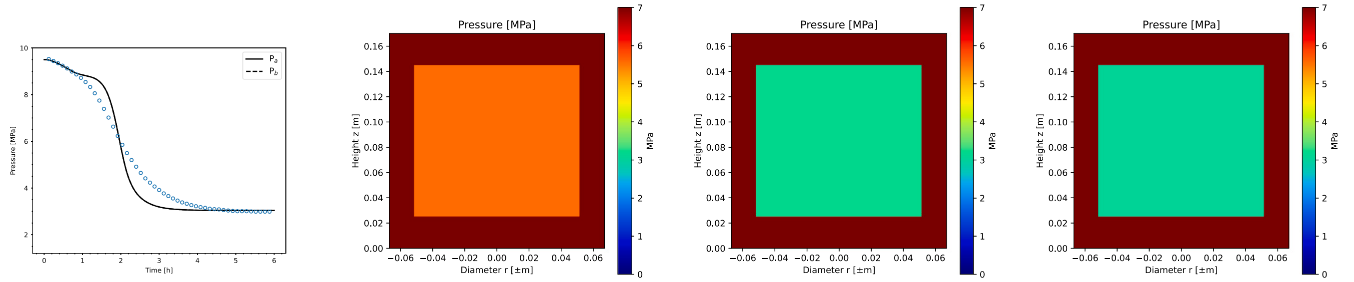

Pressure — time evolution
(a)

Pressure — spatial distributions at 2 h, 3 h, 5 h
(b)

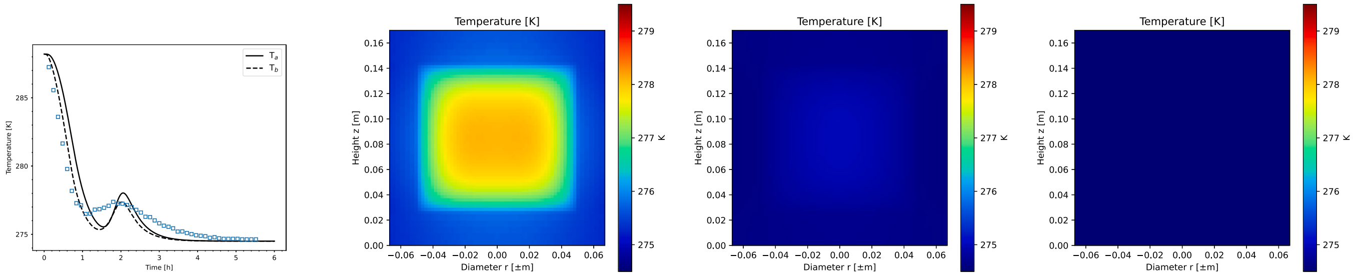

Temperature — time evolution
(c)

Temperature — spatial distributions at 2 h, 3 h, 5 h
(d)

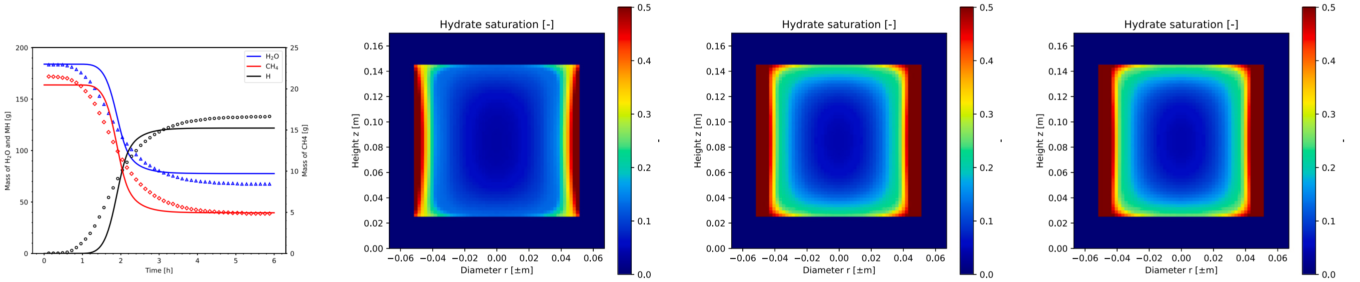

Mass — time evolution
(e)

Hydrate — spatial distributions at 2 h, 3 h, 5 h
(f)

Fig. 3. Results for CH_4-hydrate formation experiment after 6 h of simulation. (Left) Time evolution of (a) pressure, (c) temperature at sensors a and b and (e) total mass of H_2O, CH_4 and MH components. (Right) Spatial distributions of (b) pressure, (d) temperature and (f) hydrate saturation at different times. Markers show reference points from Reference [8].

(side, top, bottom) are impermeable to flow and held isothermal at the external bath temperature ($T_b = 1.0\,°C$). The core is pressurized from the gas cap by pressure-controlled CO_2 injection at $P_{inj} = 3.20\,MPa$ and $T_{inj} = 1.0\,°C$. The rate of formation follows the CO_2-specific kinetic law [53] mentioned in Table 2. Capillary pressure, relative permeability and porosity-permeability relationship are taken from Reference [22] mentioned in Section 2.4.

Fig. 5 shows the temporal evolution of pressure and temperature at different locations in the core. While pressure remains virtually constant throughout the process, the temperature strongly increases at early stages due to the exothermic process of hydrate formation. The temperature increase is more pronounced at the top and middle sensors, indicating that the amount of hydrate formed in these regions is larger than in the bottom, where no cooling is applied. After equilibration, a uniform temperature distribution is restored due to conductive fluxes from the cooling bath inward.

The features that show up in the time data can be recognized in the spatial maps from Fig. 6. In addition, it can be observed that the cooling bath enforces low temperatures from the outside and the temperature increase that accompanies the formation process is suppressed at the outer region. The strongest driving force for hydrate formation is thus induced at the outermost cells, resulting in a non-uniform final hydrate saturation.

4.2. Dissociation of CH_4 – hydrates

Here, we run test cases of hydrate dissociation in hydrate-bearing sedimentary layers. We follow two scenarios from Reference [30]. Case A considers thermal stimulation to induce hydrate dissociation by providing a heat source at the well at the centre of the reservoir to bring the temperature above hydrate equilibrium conditions. In case B, hydrate dissociation is driven by depressurization, where the pressure at the well is reduced below the hydrate equilibrium pressure. Both cases are concerned with so-called Class 3 type radial reservoirs, hydrate accumulations that are underlain and overlain by impermeable layers [54]. Table 4 lists the specifics. The dissociation of CH_4-hydrates follows a similar kinetic model as the formation case listed in Table 2.

4.2.1. Case A: thermal stimulation

Test case A concerns a radial domain in which the size of the grid blocks increases in the radial direction, starting from a characteristic

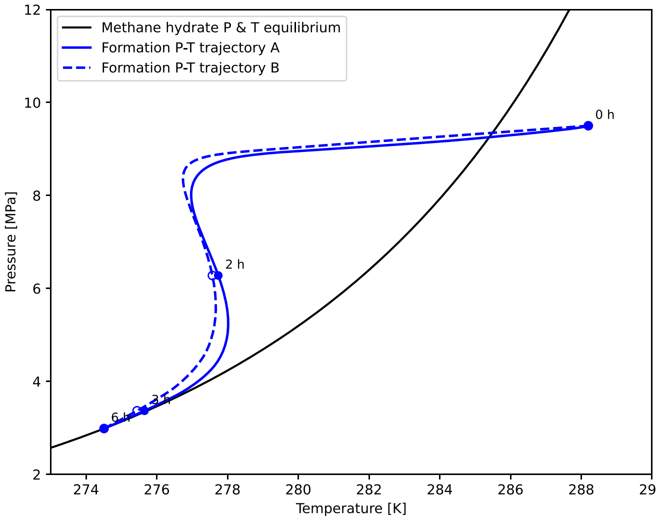

Fig. 4. Pressure–temperature trajectories at sensors A and B during CH_4-hydrate formation, compared with the CH_4-hydrate equilibrium curve. Markers indicate system conditions at 0, 2, 3, and 6 h.

Table 4
Parameters for simulation of dissociation test cases A and B.

Parameter	Case A	Case B
Thickness	10 m	10 m
Radius	1000 m	10000 m
P_{init}	40 bar	90 bar
T_{init}	1.0 °C	11.0 °C
P_{well}	40 bar	27 bar
T_{well}	45.0 °C	N/A
$S_{h,init}$	0.5	0.5
$S_{a,init}$	0.5	0.5
$S_{g,init}$	0.0	0.0
Porosity ϕ	0.30	
Permeability k	296 mD	
Density of rock ρ_r	2600 kg/m^3	
Thermal conductivity of dry rock κ_d	0.5 W/m K	
Thermal conductivity of wet rock κ_w	3.1 W/m K	
Heat capacity of rock $c_{p,r}$	1000 J/kg K	

length of 5 cm at the well radius $r_w = 7.5$ cm, to 100 m at the outer radius of 1000 m. The domain consists of a single layer with a thickness of 10 m.

Initially, two-phase brine-hydrate equilibrium exists, with saturations of aqueous and hydrate phases equal at $S_h = S_a = 0.50$, uniform throughout the domain. Temperature and pressure are both specified at 274.15 K and 40.0 bar. The pressure at the well is kept at the initial pressure, and production is initialized by increasing the temperature at the well to the specified $T_w = 45$ °C.

The results of test case A after 30 days of simulation time are displayed in Fig. 7. A fine OBL resolution of 4000 points has been used. Figures (a) and (b) respectively show the spatial distributions of pressure and temperature and phase saturations. A temperature front propagates into the reservoir, resulting in a small zone behind which the hydrates have completely dissociated. In the simulations, the temperature rapidly decreases from well temperature $T_w = 45$ °C into the near-well region, in part due to the endothermic nature of hydrate dissociation and the increasingly large area of dissociating hydrates outwards. The largest pressure can be found in the dissociation zone, leading to fluid flow in both the inward and outward directions. The amount of gas produced in the early stages, however, is insignificant. Ahead of the dissociation front, secondary hydrate formation occurs as a result of the increased pressure associated with gas release from dissociation.

4.2.2. *Case B: depressurization*

The second test case is very similar to case A, but now dissociation is triggered by constant pressure at the well. Initial saturations are again uniformly distributed $S_h = S_a = 0.50$ with a temperature and pressure defined at 284.15 K and 90.0 bar, respectively. Production is initialized with a constant pressure control at the well at 27.0 bar.

The results of test case B after 30 days of simulation time are displayed in Fig. 8. An OBL resolution of 401 points has been used. Figures (a) and (b) show the spatial distributions of pressure and temperature and phase saturations, respectively. It can be observed that the depressurization technique results in a wide region of dissociating hydrates, unlike in case A. Temperature decreases due to the combined effect of endothermic dissociation and expansion cooling of the released gas.

The temperature distribution shows an increase close to the well. This is likely to be related to the reaction rate for small concentrations of the hydrate component. The reaction rate is governed by the hydrate surface area, for which the exponent in Table 2 introduces severe nonlinearities that the OBL parametrization is not able to fully resolve. Further illustration of this effect can be found in Appendix B, where the temperature increase becomes slightly more pronounced with lower OBL resolutions.

4.3. *Discussion on simulation results*

A simulation model for hydrate formation and dissociation must be able to capture the competing physical phenomena – a sharp decrease in temperature due to the boundary conditions, adiabatic cooling, exothermic hydrate formation reaction, and a reaction rate highly sensitive to hydrate surface area – which result in highly nonlinear simulation problems. This requires an appropriate resolution of the OBL mesh. A coarse resolution of the OBL mesh is not fully able to resolve the nonlinearities introduced by the kinetic reaction. A very fine resolution would be a limiting performance factor, thereby losing the advantages of the OBL approach. In our experience, a one-dimensional simulation is usually sufficient to get a good grasp of the accuracy that is required to capture the physical behaviour and no extensive numerical studies have to be performed. The OBL technique, in the end, provides an approximation of the actual physics where no mathematical inconsistencies are introduced and a reasonably accurate approximation quickly approaches a full-physics solution.

In addition, the default uniformity of the parameter space parametrization may need to be addressed to make optimal use of OBL in thermodynamic regions where it is most sensitive. We have ongoing developments to introduce nested interpolation for exactly this kind of problems, where most changes occur in a small range of the thermodynamic parameter space (e.g., acids, ions and kinetic rates).

To illustrate how OBL- and grid resolution affect scaling and performance, we perform a convergence analysis for the CO_2-hydrate formation case and CH_4 dissociation case B (Appendix B). OBL statistics show that Jacobian assembly increasingly dominates the runtime with finer OBL resolution (Table B.5). This is due to a higher amount of points to be generated, while the number of interpolations remain of the same order of magnitude. In addition, diagnostics of the grid convergence study (Table B.6) indicate a good scalability of the OBL technique with grid resolution. This is due to the fact that the number of interpolations increases rapidly with the number of primary unknowns, while the amount of points generated remains orders of magnitude less. This presents a significant computational advantage over conventional simulators that utilize analytical or numerical derivatives for Jacobian assembly, which scale poorly with the number of unknowns. A similar conclusion was drawn from a comparison between TOUGH2 and open-DARTS [55].

Across all cases, the dominant sensitivities remain the kinetic constants and activation energy together with the geometric surface term (A_s, r_p, F_A). The patterns of hydrate formation and dissociation, as well

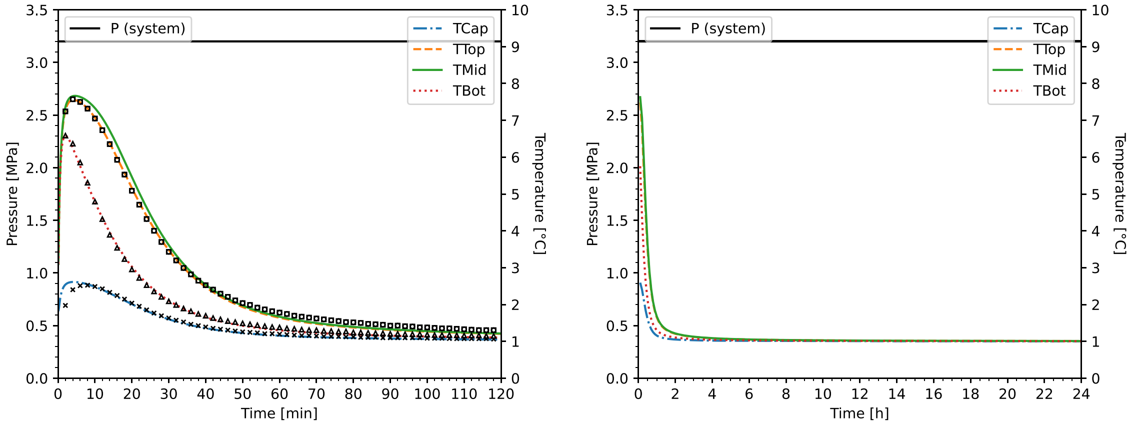

(a) (b)

Fig. 5. Time evolution of pressure and temperature at sensors at bottom, middle, top and gas cap after (a) 2 h and (b) 24 h of simulation of CO_2-hydrate formation experiment. Markers show reference points from Reference [22].

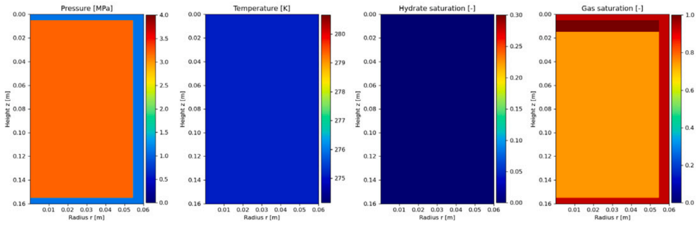

(a) t = 0 min

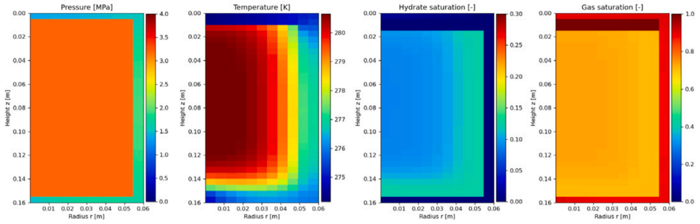

(b) t = 3 min

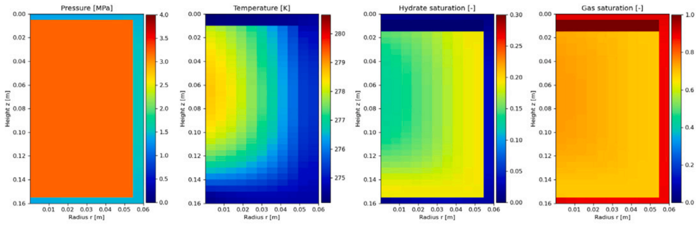

(c) t = 20 min

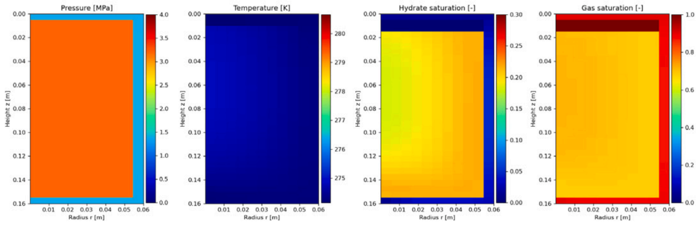

(d) t = 120 min

Fig. 6. Spatial distribution of pressure, temperature and gas/hydrate saturations after (a) *t* = 0 min, (b) *t* = 3 min, (c) *t* = 20 min and (d) *t* = 120 min of simulation of CO_2-hydrate formation experiment.

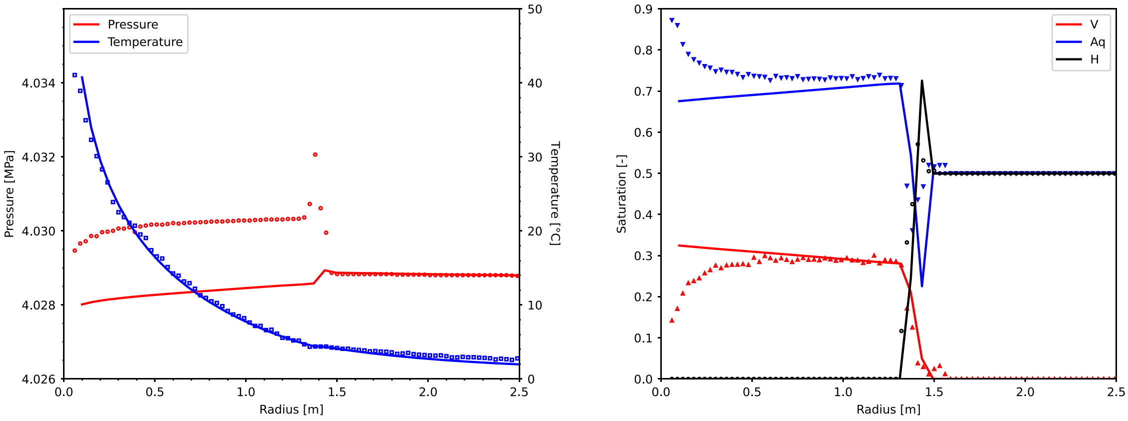

(a) (b)

Fig. 7. Results for case A after 30 days of simulation. Spatial distributions of (a) pressure and temperature and (b) saturations of V, Aq and H phases. Markers show reference points from Reference [30].

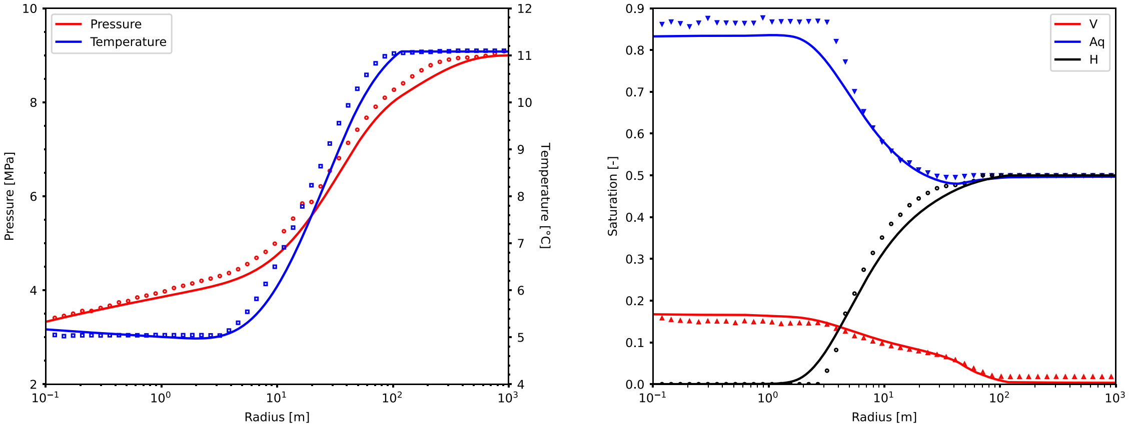

(a) (b)

Fig. 8. Results for case B after 30 days of simulation. Spatial distributions of (a) pressure and temperature and (b) saturations of V, Aq and H phases. Markers show reference points from Reference [30].

as pressure and temperature evolution, prove to be highly dependent on the input parameters of the kinetic rates. A small adjustment in the inputs for the formation study resulted in significantly different hydrate distributions throughout the core. Capillary effects and residual saturations mainly modulate phase redistribution and heat removal without changing the qualitative trends.

A comparison between kinetic and equilibrium reaction models will be an essential step towards making the appropriate assumptions for the thermodynamic modelling of hydrate systems. Simulations under equilibrium conditions would be less affected by the issues addressed here. For an equilibrium model, however, it is preferable to solve the governing equations with enthalpy as a state variable, as the number of phases at the hydrate equilibrium curve exceeds the number of components, and a *PT*-flash is not able to resolve that. Yet, if an equilibrium approach is reasonably accurate, this would be a significant benefit for the simulation of more complex fluid mixtures and multi-component, multi-type hydrates.

5. Conclusions

In this work, we presented a kinetic simulation model for gas hydrates in porous media. We used a thermal-compositional formulation that is capable of treating the conservation of mass and energy in a unified manner. The implementation of advanced thermodynamic models and hydrate formation and dissociation under kinetic assumptions was simplified through the use of the Operator-Based Linearization technique. This method provides flexibility for physical modelling and effectively captures the complex physics of gas hydrates in porous media.

We demonstrated the applicability of the simulation framework for CH_4- and CO_2-hydrate formation experiments at the core scale, as well as field-scale scenarios for gas production from CH_4-hydrates by thermal stimulation and depressurization. The interaction of a range of thermal-compositional phenomena, such as phase changes, adiabatic expansion, kinetic rates and reaction enthalpy, gives rise to highly nonlinear physics which an appropriate OBL discretization is able to resolve.

CRediT authorship contribution statement

Michiel Wapperom: Writing – original draft, Validation, Software, Methodology, Investigation, Formal analysis, Conceptualization. **Sadegh M. Taghinejad:** Writing – review & editing, Validation, Software, Methodology, Investigation, Formal analysis, Conceptualization. **Xiaocong Lyu:** Writing – review & editing, Validation, Software. **Rouhi**

Farajzadeh: Writing – review & editing, Methodology, Funding acquisition. **Denis Voskov:** Writing – review & editing, Supervision, Project administration, Methodology, Funding acquisition, Conceptualization.

Declaration of competing interest

The authors declare that they have no known competing financial interests or personal relationships that could have appeared to influence the work reported in this paper.

Acknowledgements

The authors would like to acknowledge TotalEnergies and Shell Global Solutions International for financial support.

Appendix A. Hydrate EoS

The statistical thermodynamic model from Reference [49] derives the fugacity of water in the hydrate phase by comparing the energy change from an empty hydrate lattice to an occupied hydrate phase with the energy change to an aqueous phase:

$$f_{w,H} = f_{w,A} \exp\left[\frac{\Delta\mu_{w,H} - \Delta\mu_{w,A}}{RT}\right] \tag{A.1}$$

The free energy change of water due to the occupation of hydrate cages is related through

$$\frac{\Delta\mu_{w,H}}{RT} = \frac{\mu_{w,H}}{RT} - \frac{g_{w,\beta}}{RT} = \sum_{m} \nu_m \ln\left(1 - \sum_{j} \theta_{jm}\right) \tag{A.2}$$

where $g_{w,\beta}$ is the chemical potential of water in the empty standard hydrate lattice at a given volume, ν_m is the number of cavities of type m divided by the number of water molecules in the unit cell and θ_{jm} is the fractional occupancy of cage m by component j, given as

$$\theta_{jm} = \frac{C_{jm} f_j}{1 + \sum_k C_{km} f_k} \tag{A.3}$$

where f_j is the fugacity of guest molecule j and C_{jm} is the Langmuir adsorption constant of component j in cavity m, describing the potential interaction between the encaged guest molecules and the water molecules surrounding it. The Langmuir constants are taken from Reference [50] and assume a Kihara cell potential. Hydrate composition can be derived from (A.3) by:

$$x_{iH} = \frac{\sum_m \nu_m \theta_{im}}{1 + \sum_m \sum_j \nu_m \theta_{jm}} \tag{A.4}$$

and water mole fraction is equal to $x_{wH} = 1 - \sum_j x_{jH}$.

In the original $VdWP$ model, the fugacity of water must be known. In order to eliminate this constraint in model development, Reference [50] suggested not to develop a relation between the chemical potential of water in an aqueous phase and standard empty hydrate lattice, but to use the standard state of water in ideal gas state at 1 bar:

$$f_{w,H} = f_{io} \exp\left[\frac{\mu_{w,H} - g_{wo}}{RT}\right] \tag{A.5}$$

Here, f_{io} is equal to 1 bar and g_{wo} is the Gibbs energy of water in the ideal gas state at 1 bar and the chemical potential of water in the hydrate $\mu_{w,H}$ appears in (A.2). In order to have a standalone expression for hydrate fugacity from (A.2), Reference [50] derived the Gibbs energy of the hypothetical empty hydrate lattice using pure component thermodynamics:

$$\frac{g_{w,\beta}}{RT} = \frac{g_{w_0,\beta}}{RT_0} - \int_{T_0}^{T} \frac{h_{w,\beta}}{RT^2}\, dT + \int_{P_0}^{P} \frac{v_{w,\beta}}{RT}\, dP \tag{A.6}$$

Expressions for the terms in (A.2), (A.3) and (A.6) have been derived for the standard state in Reference [50].

Appendix B. Convergence analysis

B.1. Effect of OBL resolution

We perform a convergence analysis for the CO_2-hydrate formation case and the depressurization case with regard to OBL resolution. We consider different numbers of OBL points along each axis.

The results of test case B after 30 days of simulation are displayed in Fig. B.9. Figures (a) and (b) respectively show the spatial distributions of pressure and temperature and phase saturations for different resolutions. For the intermediate OBL resolution ($n = 401$), the solution closely approaches the finest case ($n = 40001$): pressure and phase-saturation profiles are essentially indistinguishable at the plotting scale, and temperature profiles differ only in a small region near the well. As discussed in Section 4.2.2, the temperature field close to the well is more sensitive to resolution because steep thermal gradients and strong coupling to phase change amplify interpolation errors. A second, resolution-dependent effect originates from how initial equilibrium is represented within the discrete OBL space. Because properties are interpolated on the OBL grid, "exact" equilibrium can be realized at slightly offset states relative to a continuous description; for hydrates this appears as a small shift of the effective equilibrium curve and initial saturations. The coarser the OBL grid, the more pronounced this shift; refining to $n = 401$ largely removes it, and at $n = 40001$ it is negligible for this case.

In practice, we find that $n = 401$ provides a grid-independent solution for case B at 30 days while remaining economical. Finer OBL tables (e.g., $n = 4001$ points) are supported and converge, but the remaining differences relative to $n = 401$ are minor for the diagnostics shown. If longer production windows or stronger thermal/pressure transients are considered, a higher OBL resolution may be warranted to control near-well temperature sensitivity; conversely, too low a resolution can degrade the initialization and slow nonlinear convergence. This indicates a problem-specific threshold OBL resolution: below this threshold the tables are too coarse and introduce visible artefacts, while above it further refinement mainly increases CPU time and only slightly modifies the solution.

Table B.5 presents the simulation diagnostics for the one-dimensional CH_4 dissociation case B and 2D CO_2 formation case. The table summarizes the total CPU time, time spent in Jacobian assembly, and OBL statistics (number of interpolations and points generated) for different OBL resolutions. For the CO_2-hydrate formation case, increasing the number of OBL points from 401 to 4 001 and 40 001 leads to a strong increase in CPU time (from tens of seconds to several thousand seconds), while the total number of interpolations changes only weakly. A similar behaviour is observed for case B, where refining the OBL resolution from 201 to 401 and 4 001–40 001 points increases the runtime by up to two orders of magnitude. In all runs, the number of interpolations is much larger than the number of points generated, indicating that the operators are reused extensively and the extra cost of generating new points is small when averaged over the many interpolations.

B.2. Effect of grid spacing for case B

Here, we analyse the sensitivity of case B to the radial grid spacing using uniform grids with $\Delta r = 0.2$, 1 and 4. The corresponding statistics are given in Table B.6. As Δr increases, the total CPU time decreases from about 5×10^2 s to a few tens of seconds and the number of interpolations drops by more than an order of magnitude, reflecting the reduction in the number of grid cells. As expected, coarser grids progressively smooth the near-well gradients and reduce the spatial resolution of pressure, temperature and saturation profiles, while the finest grid ($\Delta r = 0.2$) resolves the sharp behaviour best at the highest computational cost. Together with the OBL-resolution study above, this confirms the usual accuracy–cost trade-off and shows that, for this benchmark, one can select a grid spacing just fine enough to capture the near-well behaviour without unnecessary cost.

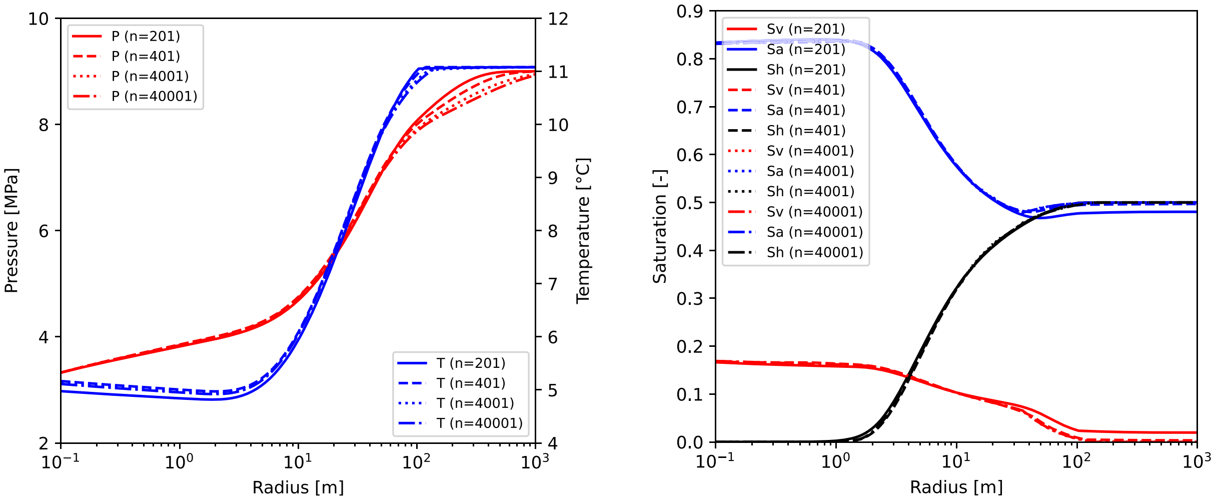

(a) (b)

Fig. B.9. Results for case B after 30 days of simulation for four OBL resolutions: 200, 400, and 600 points. Spatial distributions of (a) pressure and temperature and (b) saturations of V, Aq, and H phases.

Table B.5

Effect of OBL resolution (number of OBL points N_{OBL}) on computational performance for the CO_2 formation (2D) and CH_4 depressurization (1D, case B) problems.

Case	N_{OBL}	CPU [s]	Jac. ass. [s]	Interpolations	Points gen.	Newton it. (Wasted)
CO_2-hydrate formation	401	23	14	7.23×10^7	18 200	2076 (275)
	4 001	769	760	7.27×10^7	1 280 000	1877 (457)
	40 001	7243	7228	7.39×10^7	5 950 000	1941 (661)
CH_4-hydrate dissociation (B)	201	5	3	1.20×10^7	4 153	553 (0)
	401	10	7	1.35×10^7	12 939	643 (0)
	4 001	411	404	3.08×10^7	755 816	895 (924)
	40 001	615	607	2.99×10^7	1 130 654	914 (875)

Table B.6

Effect of uniform radial grid spacing Δr on computational performance for the CH_4 depressurization case B (fixed $N_{\mathrm{OBL}} = 401$).

Δr	Total time [s]	Jacobian assembly [s]	Interpolations	Points generated	Newton it. (Wasted)
0.2	504	175	3.22×10^9	9498	856 (0)
1.0	99	35	6.10×10^8	5416	792 (0)
4.0	27	9	1.42×10^8	2983	709 (0)

Data availability

Data will be made available on request.

References

[1] Sloan Jr ED, Koh CA. Clathrate Hydrates of Natural Gases. 3rd ed.. Boca Raton: CRC Press; 2007, http://dx.doi.org/10.1201/9781420008494.

[2] Sayani J, Pedapati S, Lal B. Phase behavior study on gas hydrates formation in gas dominant multiphase pipelines with crude oil and high CO_2 mixed gas. Sci Rep 2020;10:14748. http://dx.doi.org/10.1038/s41598-020-71509-6.

[3] Oldenburg CM. Joule-thomson cooling due to CO_2 injection into natural gas reservoirs. Energy Convers Manage 2007;48:1808–15. http://dx.doi.org/10.1016/j.enconman.2007.01.010.

[4] Aghajanloo M, Yan L, Berg S, Voskov D, Farajzadeh R. Impact of CO_2 hydrates on injectivity during CO_2 storage in depleted gas fields: A literature review. Gas Sci Eng 2024;123:205250. http://dx.doi.org/10.1016/j.jgsce.2024.205250.

[5] Klauda JB, Sandler SI. Global distribution of methane hydrate in ocean sediment. Energy & Fuels 2005;19(2):459–70. http://dx.doi.org/10.1021/ef049798o.

[6] Boswell R, Collett TS. Current perspectives on gas hydrate resources. Energy & Environ Sci 2011;4:1206–15. http://dx.doi.org/10.1039/C0EE00203H.

[7] Ruppel C, Kessler J. The interaction of climate change and methane hydrates. Rev Geophys 2017;55(1):126–68. http://dx.doi.org/10.1002/2016RG000534.

[8] Yin Z, Moridis GJ, Kiang Tan H, Linga P. Numerical analysis of experimental studies of methane hydrate formation in a sandy porous medium. Appl Energy 2018;220:681–704. http://dx.doi.org/10.1016/j.apenergy.2018.03.075.

[9] Zhao J, Xu K, Song Y, Liu W, Lam W, Liu Y, Xue K, Zhu Y, Yu X, Li Q. A review on research on replacement of CH_4 in natural gas hydrates by use of CO_2. Energies 2012;5(2):399–419. http://dx.doi.org/10.3390/en5020399.

[10] Dance T. Assessment and geological characterisation of the CO2CRC otway project CO2 storage demonstration site: From prefeasibility to injection. Mar Pet Geol 2013;46:251–69. http://dx.doi.org/10.1016/j.marpetgeo.2013.06.008, URL https://www.sciencedirect.com/science/article/pii/S0264817213001529.

[11] Oldenburg CM, Benson SM. CO2 injection for enhanced gas production and carbon sequestration. SPE Int Pet Conf Exhib Mex 2002. http://dx.doi.org/10.2118/74367-MS.

[12] House KZ, Schrag DP, Harvey CF, Lackner KS. Permanent carbon dioxide storage in deep-sea sediments. Proc Natl Acad Sci 2006;103(33):12291–5. http://dx.doi.org/10.1073/pnas.0605318103.

[13] Soloviev V, Ginsburg GD. Formation of submarine gas hydrates. Bull Geol Soc Den 1994;41:86–94. http://dx.doi.org/10.37570/BGSD-1995-41-09, URL https://www.researchgate.net/publication/242259825_Formation_of_submarine_gas_hydrates.

[14] Anderson BJ, Boswell R, Collett TS, Farrell H, Ohtsuka S, White MD. Review of the findings of the Ignik Sikumi CO_2-CH_4 gas hydrate exchange field trial. In: 8th International conference on gas hydrates (ICGH8-2014). 2014.

[15] Yamamoto K, Boswell R, Collett TS, Dallimore SR, Lu H. Review of past gas production attempts from subsurface gas hydrate deposits and necessity of long-term production testing. Energy & Fuels 2022;36:5047–62. http://dx.doi.org/10.1021/acs.energyfuels.1c04119.

[16] Aghajanloo M, Taghinejad SM, Voskov D, Farajzadeh R. Influence of water saturation and water memory on CO2 hydrate formation/dissociation in porous media under flowing condition. Chem Eng J 2024;492. http://dx.doi.org/10.1016/j.cej.2024.152455.

[17] Aghajanloo M, Jones S, Yan L, Voskov D, Farajzadeh R. Evaluation of CO2 hydrate saturation in porous core experiments using medical CT images. Energy & Fuels 2024;38(12):11037–42. http://dx.doi.org/10.1021/ACS.ENERGYFUELS.4C01537, URL.

[18] Moridis G. User's manual for the HYDRATE v1.5 option of TOUGH+ v1.5: a code for the simulation of system behaviour in hydrate-bearing geologic media. 2014, URL https://tough.lbl.gov/assets/files/02/documentation/TH_Manual_v1.5s.pdf.

[19] CMG STARS. Computer Modeling Group Ltd, Calgary, Alberta, Canada, 2007. 2023, https://www.cmgl.ca/stars. [Accessed: 23 July 2023].

[20] Konno Y, Masuda Y, Oyama H, Kurihara M, Ouchi H. SS - Gas Hydrate:Numerical Analysis on the Rate-Determining Factors of Depressurization-Induced Gas Production from Methane Hydrate Cores. 2010, http://dx.doi.org/10.4043/20591-MS.

[21] Yonkofski CM, Horner JA, White MD. Experimental and numerical investigation of hydrate-guest molecule exchange kinetics. J Nat Gas Sci Eng 2016;35:1480–9. http://dx.doi.org/10.1016/J.JNGSE.2016.03.080, URL https://www.sciencedirect.com/science/article/pii/S187551001630186X.

[22] Li G, Englezos P, Sun D, Li X-S, Lv Q-N, Weng Y-F. Simulation of CO_2 hydrate formation in porous medium and comparison with laboratory trial data. Energy 2024;304:133224. http://dx.doi.org/10.1016/j.energy.2024.133224.

[23] Moridis G, Moridis GJ, Kowalsky MB, Pruess K. TOUGH+Hydrate v1.0 user's manual: A code for the simulation of system behavior in hydrate-bearing geologic media. Technical report, United States; 2008, http://dx.doi.org/10.2172/927149, https://www.osti.gov/biblio/927149, https://www.osti.gov/servlets/purl/927149.

[24] Voskov D, Saifullin I, Novikov A, Wapperom M, Orozco L, Seabra GS, Chen Y, Khait M, Lyu X, Tian X, de Hoop S, Palha A. Open delft advanced research terra simulator (open-DARTS). J Open Source Softw 2024;9(99):6737. http://dx.doi.org/10.21105/joss.06737.

[25] Khait M, Voskov DV. Adaptive parameterization for solving of thermal/compositional nonlinear flow and transport with buoyancy. SPE J 2018;23(02):522–34. http://dx.doi.org/10.2118/182685-PA.

[26] Wang Y, Voskov D, Khait M, Bruhn D. An efficient numerical simulator for geothermal simulation: A benchmark study. Appl Energy 2020;264. http://dx.doi.org/10.1016/j.apenergy.2020.114693.

[27] Kala K, Voskov DV. Element balance formulation in reactive compositional flow and transport with parameterization technique. Comput Geosci 2020;24(2):609–24. http://dx.doi.org/10.1007/s10596-019-9828-y.

[28] Lyu X, Voskov D. Advanced modeling of enhanced CO_2 dissolution trapping in saline aquifers. Int J Greenh Gas Control 2023;127:103907. http://dx.doi.org/10.1016/j.ijggc.2023.103907.

[29] Wapperom M, Lyu X, Nichita D, Voskov D. A unified thermal-reactive compositional simulation framework for modeling CO_2 sequestration at various scales. 2023, http://dx.doi.org/10.2118/212182-MS.

[30] Kowalsky MB, Moridis GJ. Comparison of kinetic and equilibrium reaction models in simulating gas hydrate behavior in porous media. Energy Convers Manage 2007;48(6):1850–63. http://dx.doi.org/10.1016/j.enconman.2007.01.017.

[31] Khait M, Voskov DV. Operator-based linearization for general purpose reservoir simulation. J Pet Sci Eng 2017;157:990–8. http://dx.doi.org/10.1016/j.petrol.2017.08.009.

[32] Voskov DV. Operator-based linearization approach for modeling of multiphase multi-component flow in porous media. J Comput Phys 2017;337:275–88. http://dx.doi.org/10.1016/j.jcp.2017.02.041.

[33] Lyu X, Khait M, Voskov D. Operator-based linearization approach for modelling of multiphase flow with buoyancy and capillarity. SPE J 2021;1–18. http://dx.doi.org/10.2118/205378-PA.

[34] Genuchten MTv. A closed-form equation for predicting the hydraulic conductivity of unsaturated soils. Soil Sci Am J 1980;44(5):892–8. http://dx.doi.org/10.2136/SSSAJ1980.03615995004400050002X, https://onlinelibrary.wiley.com/doi/abs/10.2136/sssaj1980.03615995004400050002x, https://acsess.onlinelibrary.wiley.com/doi/10.2136/sssaj1980.03615995004400050002x.

[35] Bouillot B, Herri J-M. Framework for clathrate hydrate flash calculations and implications on the crystal structure and final equilibrium of mixed hydrates. Fluid Phase Equilib 2016;413:184–95. http://dx.doi.org/10.1016/j.fluid.2015.10.023.

[36] Wapperom M, dos Santos Heringer J, Nichita D, Voskov D. A hybrid-eos approach for multiphase pressure-based equilibrium calculations of reservoir mixtures with brine. Gas Sci Eng 2025.

[37] Petitfrere M, Nichita D. A comparison of conventional and reduction approaches for phase equilibrium calculations. Fluid Phase Equilib 2015;386:30–46. http://dx.doi.org/10.1016/j.fluid.2014.11.017.

[38] Petitfrere M, Nichita D. Multiphase equilibrium calculations using a reduction method. Fluid Phase Equilib 2015;401:110–26. http://dx.doi.org/10.1016/j.fluid.2015.05.006.

[39] Baker LE, Pierce AC, Luks KD. Gibbs energy analysis of phase equilibria. SPE J 1982;22(5):731–42. http://dx.doi.org/10.2118/9806-PA.

[40] Iranshahr A, Voskov D, Tchelepi H. Gibbs energy analysis: Compositional tie-simplex space. Fluid Phase Equilib 2012;321:49–58. http://dx.doi.org/10.1016/j.fluid.2012.02.001.

[41] Michelsen ML. The isothermal flash problem. Part I. Stability. Fluid Phase Equilib 1982;9:1–19. http://dx.doi.org/10.1016/0378-3812(82)85001-2.

[42] Nichita DV, Leibovici CF. A rapid and robust method for solving the rachford–rice equation using convex transformations. Fluid Phase Equilib 2013;353:38–49. http://dx.doi.org/10.1016/j.fluid.2013.05.030.

[43] Akinfiev NN, Diamond LW. Thermodynamic description of aqueous nonelectrolytes at infinite dilution over a wide range of state parameters. Geochim Cosmochim Acta 2003;67(4):613–29. http://dx.doi.org/10.1016/S0016-7037(02)01141-9.

[44] Ziabakhsh-Ganji Z, Kooi H. An equation of state for thermodynamic equilibrium of gas mixtures and brines to allow simulation of the effects of impurities in subsurface CO_2 storage. Int J Greenh Gas Control 2012;11S:S21–34. http://dx.doi.org/10.1016/j.ijggc.2012.07.025.

[45] Jager MD, Ballard AL, Sloan Jr ED. The next generation of hydrate prediction II. Dedicated aqueous phase fugacity model for hydrate prediction. Fluid Phase Equilib 2003;211:85–107. http://dx.doi.org/10.1016/S0378-3812(03)00155-9.

[46] Lundgaard L, Mollerup JM. The influence of gas phase fugacity and solubility on correlation of gas-hydrate formation pressure. Fluid Phase Equilib 1991;70(2–3):199–213. http://dx.doi.org/10.1016/0378-3812(91)85034-R.

[47] Peng D-Y, Robinson DB. A new two-constant equation of state. Ind Eng Chem Fundam 1976;15(1):59–64. http://dx.doi.org/10.1021/i160057a011.

[48] Soave G. Equilibrium constants from a modified redlich-kwong equation of state. Chem Eng Sci 1972;27:1197–203. http://dx.doi.org/10.1016/0009-2509(72)80096-4.

[49] Van der Waals JH, Platteeuw JC. Clathrate solutions. Adv Chem Phys 1958;2. http://dx.doi.org/10.1002/9780470143483.ch1.

[50] Ballard AL, Sloan Jr ED. The next generation of hydrate prediction I. Hydrate standard states and incorporation of spectroscopy. Fluid Phase Equilib 2002;194–197:371–83. http://dx.doi.org/10.1016/S0378-3812(01)00697-5.

[51] Sloan Jr ED. Clathrate hydrates of natural gases. 2nd ed.. New York: Marcel Dekker, Inc.; 1998.

[52] Yin Z, Moridis GJ, Chong ZR, Kiang Tan H, Linga P. Numerical analysis of experimental studies of methane hydrate dissociation induced by depressurization in a sandy porous medium. Appl Energy 2018;230:444–59. http://dx.doi.org/10.1016/j.apenergy.2018.08.115.

[53] Li B, Li XS, Li G. Kinetic studies of methane hydrate formation in porous media based on experiments in a pilot-scale hydrate simulator and a new model. Chem Eng Sci 2014;105:220–30. http://dx.doi.org/10.1016/J.CES.2013.11.016, URL https://www.sciencedirect.com/science/article/abs/pii/S0009250913007513.

[54] Moridis G, Collett T. Strategies for gas production from hydrate accumulations under various geological and reservoir conditions. In: TOUGH symposium. 2003.

[55] García-Navarrete LA, Guerrero FJ, Santotyo E. Scope of TOUGH2 and open-DARTS for the simulation of transport in porous-fractured media: an application to enhanced geothermal systems. Geoenergy Sci Eng 2026;258. http://dx.doi.org/10.1016/j.geoen.2025.214343.